Supplement

LA-ICP-MS data acquisition and processing

Before measurement, the surface of the resin embedded sediment was cleaned with a 200 μm-wide laser beam with a velocity of 20 μm/s. During measurements the ablated material was transported by a He-Ar carrier gas to the quadrupole ICP-MS. Operating conditions of the laser and the quadrupole ICP-MS can be found in Table S4.

Data acquisition and data reduction were carried out following the protocol given in Longerich et al. (1996) and LAMTRACE (version 2.16). The instrumental drift was assessed by measuring calibration standards at the beginning and the end of each run and linear interpolation between the respective sensitivities. The conversion from intensity signals (counts per second, cps) to concentrations (wt% and μg/g) was done using the 'BORE' command in LAMTRACE. This command converts each data point one by one and was originally designed for data analysis of single hole ablation, with possible changing concentrations with the depth of the crater. The results from LAMTRACE were further processed with MS EXCEL, normalizing to 99.9 wt%. Thereby, all concentration values below limits of detection were set to zero. From LAMTRACE, major elements were given in wt% of their oxides, and trace elements are reported in μg/g. The laser ablation timescale was then converted to a millimetre scale to obtain concentration data versus distance.

Organic geochemistry

Solvent extraction and sample cleanup

Freeze-dried sediment samples were extracted with a Dionex ASE 200 Accelerated Solvent Extraction system using a solvent mixture of DCM:MeOH (9:1).

The stainless steel extraction cells were preheated to 100ºC for 5 minutes; the solvent mixture was pumped into the cell and pressurized to 1500 psi. The samples were then extracted by flushing the extract into the collection vial. The extraction procedure was repeated 3 times for each extraction cell and finally the solvent residue was purged with nitrogen. The extracts were taken to dryness under a nitrogen stream and used to analyze chlorin concentrations. The organic extracts were then separated into two fractions using small silica columns prepared from Pasteur pipettes. The first fraction was eluted using a solvent mixture of Hexane:DCM (1:1). The second fraction was eluted using a solvent mixture of DCM:MeOH (1:1) and was used for the GDGT analysis.

Analysis of chlorins

An aliquot of the organic extracts was used to determine the concentration of chlorins using a high performance liquid chromatograph coupled to a photodiode array detector (PDA, Thermo Surveyor) (Harris and Maxwell, 1995; Fietz et al., 2011). The HPLC was operated in off-column mode with an isocratic flow of l mL min^{-1}, with a flow restrictor to stabilize the pressure. The total abundance of chlorins was measured as absorbance at 662 nm using pyropheophorbide, a methyl ester (Sigma-Aldrich), as an external standard for quantification. The total lipid extracts were taken to dryness under a gentle stream of nitrogen, sealed and stored frozen until further fractionation.

Analysis of GDGTs

GDGTs were analyzed at the Geological Institute of the ETH Zürich by high performance liquid chromatography/atmospheric pressure chemical ionization-mass spectrometry (HPLC/APCI-MS) (Hopmans et al., 2000), using a Thermo Surveyor

HPLC system coupled to an LCQ Fleet ion trap mass spectrometer. Chromatographic separation was achieved with a GRACE Prevail Cyano column (150 mm x 2.1 mm; 3 µl) maintained at 30 °C and a GRACE Prevail Cyano guard column (7.5 mm x 2.1 mm; 5 µl). The flow rate of the mobile phase was 0.3 ml min−1, and the injection volume was 10 µl. The GDGTs were eluted isocratically with a solvent mixture of the hexane:isopropanol (Hex:IPA) 1 % for the first 5 min, thereafter with a linear gradient to Hex:IPA 1.8 % IPA in 30 min, and a final column cleaning step with Hex:IPA 10 %.

Supplementary Figures

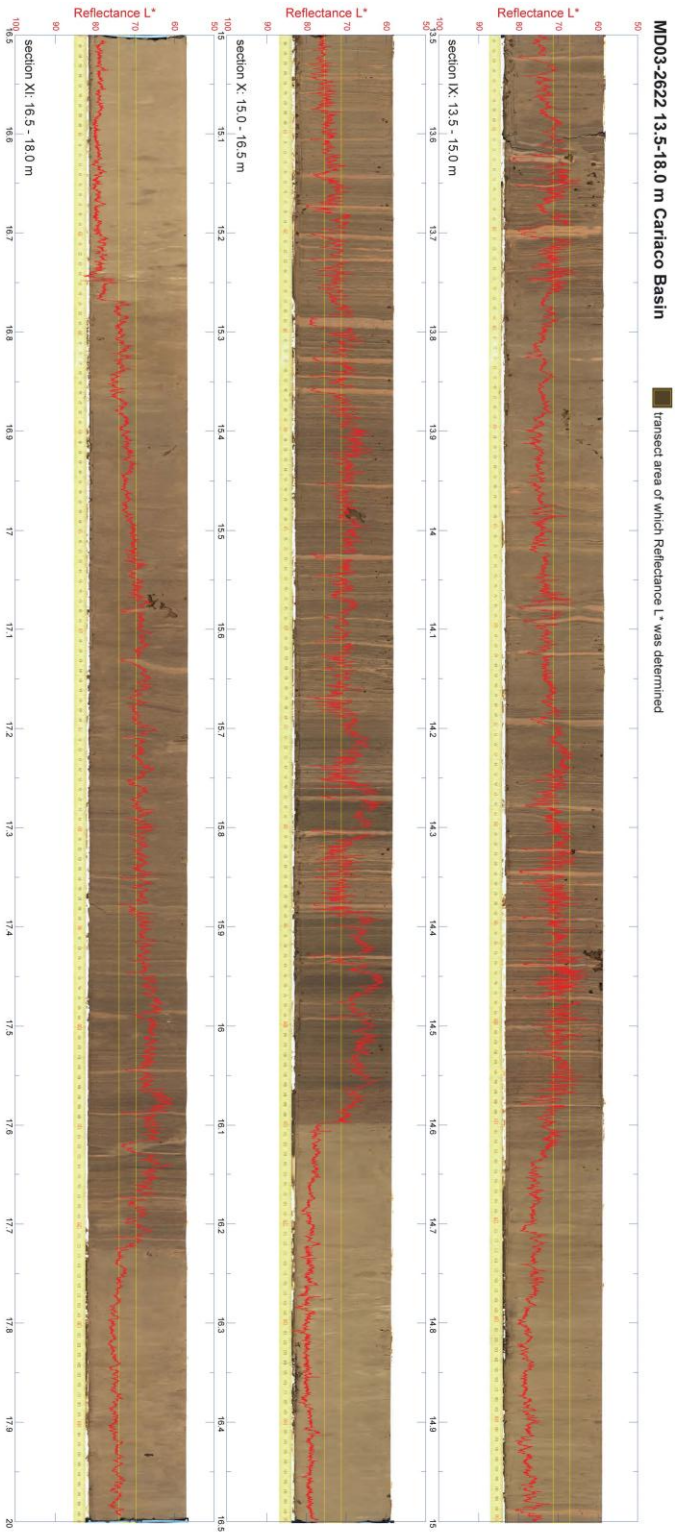

Fig. S1. Digital image of sediment surface of core MD03-2622 (13.5 - 18.0 m uncorrected depth) with total reflectance L* record (red). Areas on which L* was determined are indicated with yellow rectangles.

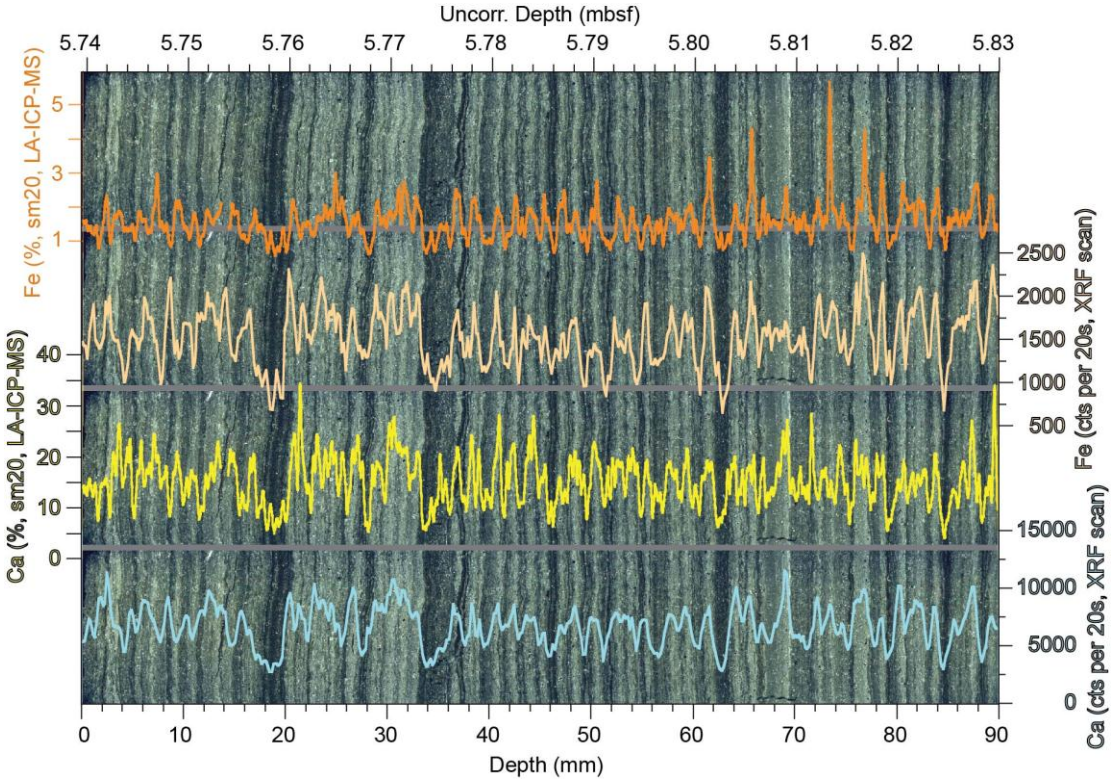

Fig. S2. Comparison of high-resolution compositional measurements acquired by LA-ICP-MS and Avaatech XRF core scanner. The pictures show the laminated section from the Younger Dryas (MD03-2621, ~5.74 - 5.83 m uncorrected depth, Fig. 4) in a thin section under cross-polarized light. The patterns in LA-ICP-MS-derived concentrations of iron (^{57}Fe, orange, 20-point running mean) and calcium (^{42}Ca, yellow, 20-point running mean) are well reproduced by intensities of Fe and Ca measured by XRF core scanner (0.2 mm resolution), even though LA-ICP-MS measurements were performed after sediment sections were embedded in resin (refer also to Fig. S3).

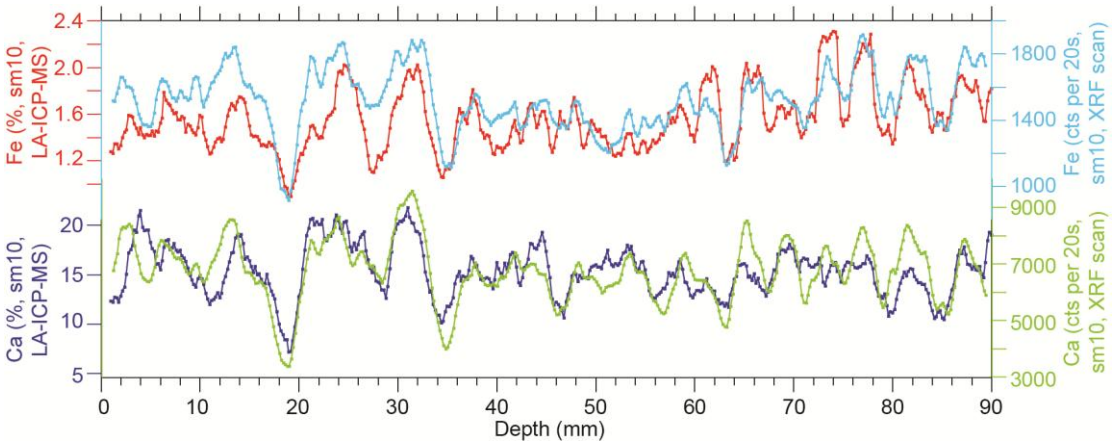

Fig. S3. Comparison of high-resolution compositional measurements acquired by LA-ICP-MS and Avaatech XRF core scanner from the Younger Dryas (MD03-2621, ~5.74 - 5.83 m uncorrected depth, Figs. 4 and S2). The LA-ICP-MS-derived concentrations of iron (^{57}Fe, dark red, 10-point running mean) and calcium (^{42}Ca, dark blue, 10-point running mean) were resampled to 0.2 mm. Intensities of Fe (light blue, 10-point running mean) and Ca (green, 10-point running mean) measured by XRF core scanner are plotted with the original sampling resolution of 0.2 mm.

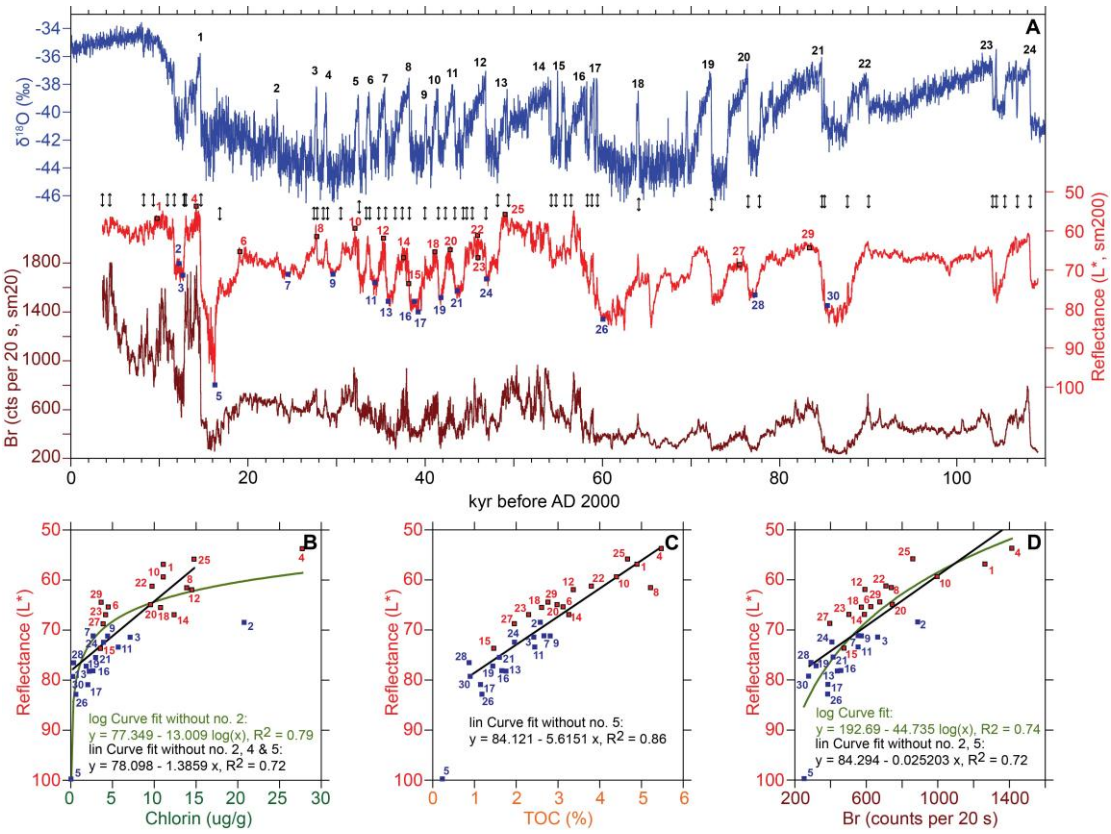

Fig. S4. Comparison of total reflectance L* with elemental bromine intensities (Br), chlorin concentrations and TOC in core MD03-2621. A) Comparison of L* (red, 200-point running mean) and Br (brown) with NGRIP record of $\delta^{18}O$ (blue) with 20-year resolution (NGRIP Members, 2004; Svensson et al., 2008; Wolff et al., 2010)). Black colored numbers indicate interstadial numbers, while the double-headed arrows indicate stratigraphic tie points. Colored numbers (red: warmer periods; blue: colder periods) indicate sampling locations for conventional XRF, chlorin, GDGTs and TOC measurements. B) to D) Cross-correlation of L* and chlorin concentrations, TOC and Br intensities. L* and Br intensities are average values corresponding to the sampling intervals.

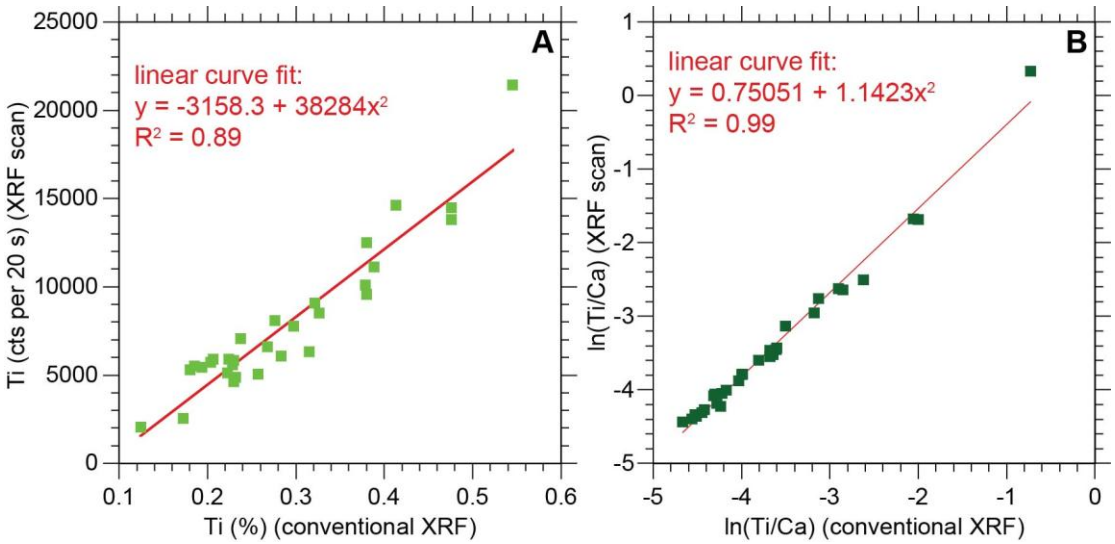

Fig. S5. Correlation of titanium (Ti) intensities with Ti concentrations. A) Ti concentrations measured with conventional XRF versus Ti intensities acquired with XRF core scanner. The Ti intensities are calculated as average values over the sampling intervals of the XRF conventional measurements. B) Comparison of log ratios ln(Ti/Ca) of intensities versus concentrations. Corresponding coefficients of determination R^2 for other major elements can be found in Tables S2 and S3.

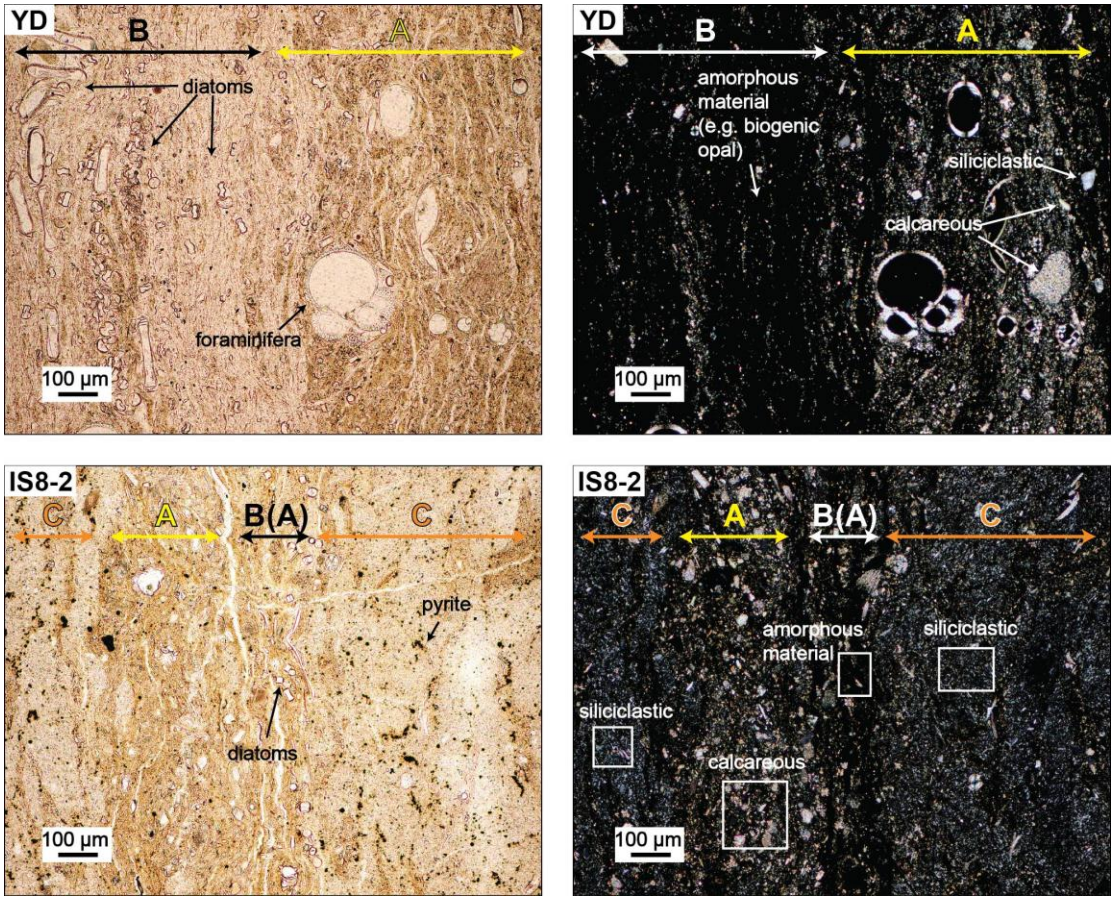

Fig. S6. Detailed view of layer types A, B and C in thin sections. The upper panels show photos of a sediment section from the Younger Dryas (Figs. 4 and 8A) under plain (left) and cross-polarized light (right). The lower panels show photos of a sediment section from the Interstadial 8 (Figs. 7 and 8C). Colored letters A (yellow), B (white) and C (orange) denote the layer types.

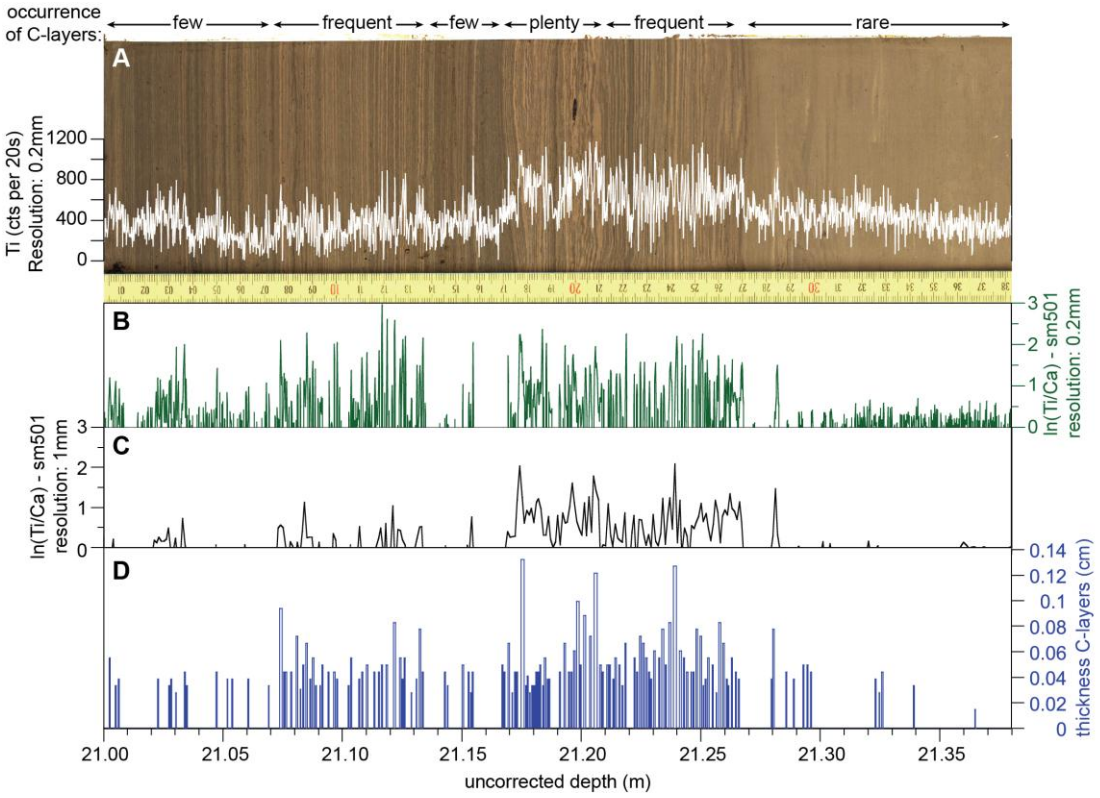

Fig. S7. Tracing C-layers with titanium (Ti) measurements (MD03-2621, 21.00 - 21.38 m uncorrected depth). A) High-resolution (0.2mm) Ti intensities record on top of a photograph of the sediment surface at the onset of Interstadial 8 (IS 8). Siliciclastic C-layers have a light orange color and are characterized by peaks in Ti intensities. B) to C) C-layers can be traced on the basis of positive peaks in the ln(Ti/Ca) time series, which was detrended by subtracting a 501- point running mean. The ln(Ti/Ca) record with the resolution of 0.2 mm (green) shows the occurrence of C-layers in greater detail than the record with 1 mm resolution (black), but the patterns are coherent. D) Thickness (cm) of C-layers approximated based on the picture and the Ti-measurements. Individual identification of the C-layers is sometimes difficult, especially if the C-layers are thin or in the stadial before IS 8, which is partly bioturbated.

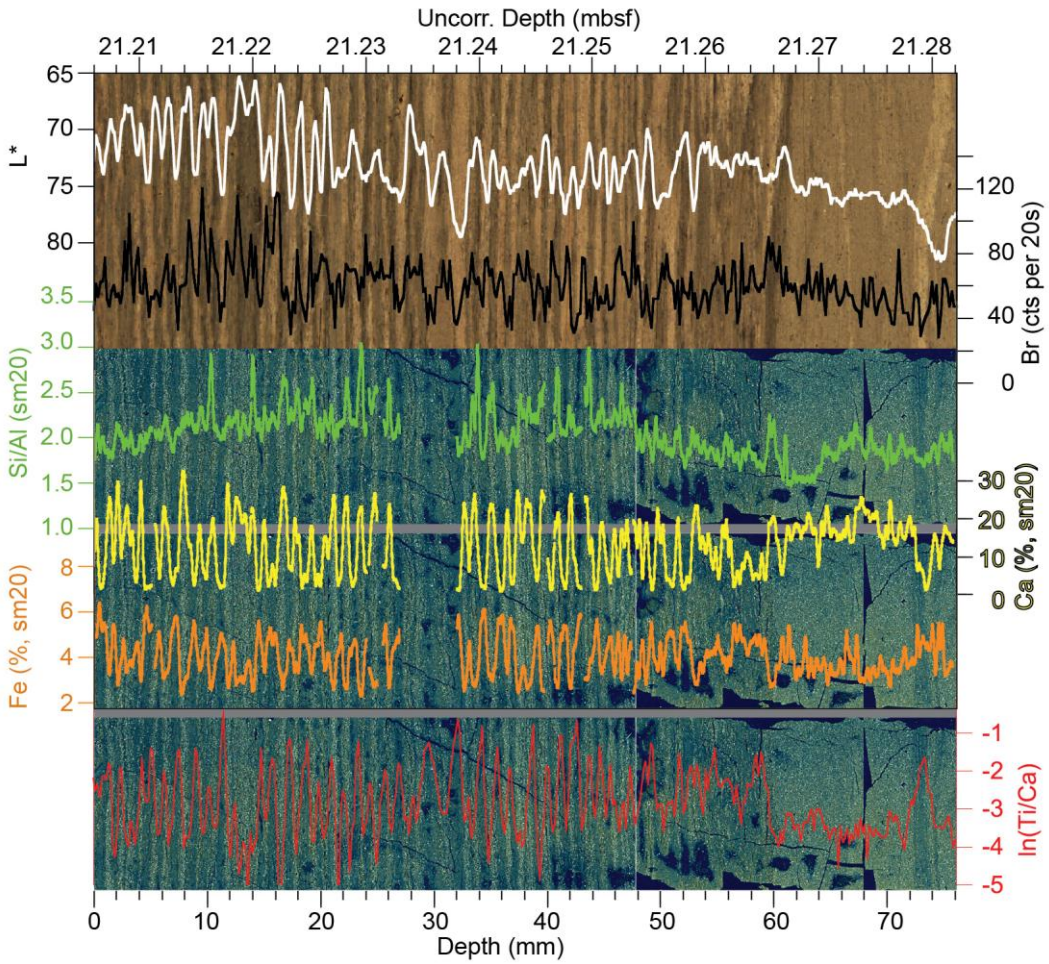

Fig. S8. Multiproxy analysis of a sediment section at the onset of Interstadial 8 (MD03-2621, ~21.206 - 21.282 m uncorrected depth). Picture types and line colors are the same as in Fig. 7 with the addition of XRF ln(Ti/Ca). Peaks in XRF ln(Ti/Ca) correspond with occurrence of C-layers (ref. Fig. 8 and Fig. S7).

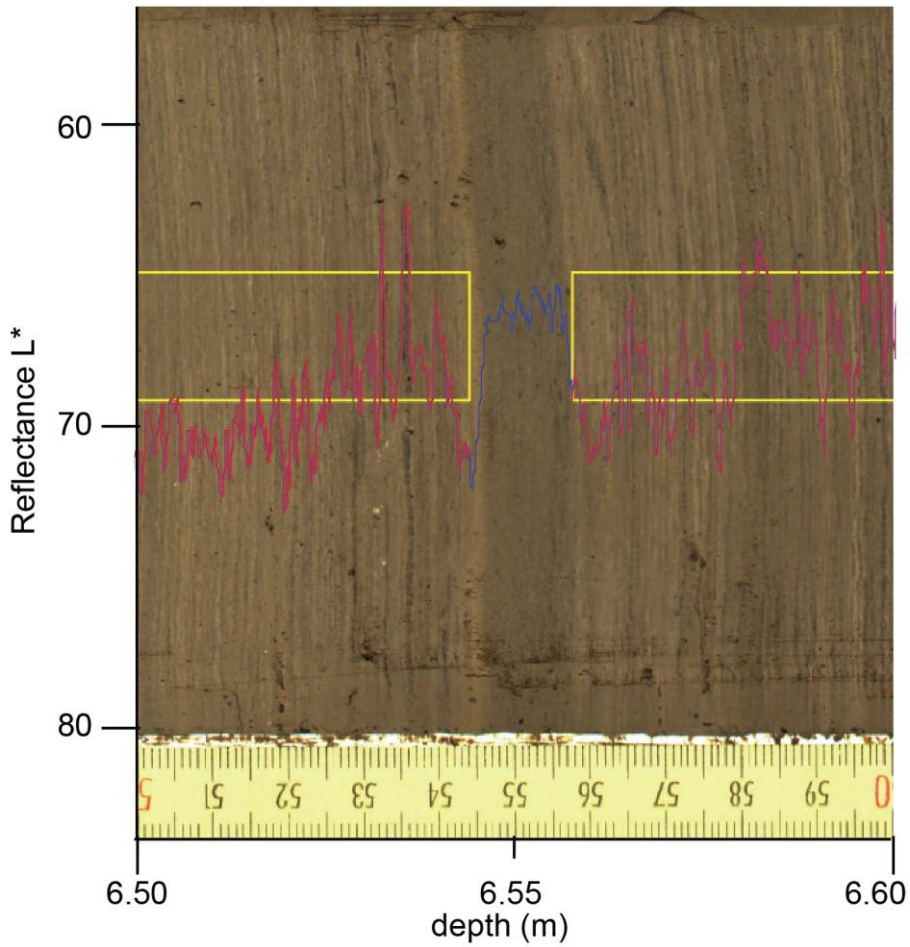

Fig. S9. Example of a turbidite in core MD03-2621 (adapted from Deplazes et al. 2013). Yellow rectangles indicate the area on which Reflectance L* (red curve) was determined. The blue curve shows L* in the section of the turbidite, that shows a trend of increasing L* from bottom to top.

Supplementary Tables

Table S1. Tiepoints for construction of age model of core MD03-2622 from the Cariaco Basin.

MD03-2622			
Corr. Depth (mbsf)	Age (a b2k)	Corr. Depth (mbsf)	Age (a b2k)
2.49592	4442.4	14.21369	34743.2
2.99701	5787.7	14.63673	35514.9
3.62884	8321.7	15.15019	36723.1
3.89729	9322.8	15.39646	36974.3
4.27256	10169.9	15.92802	37859.2
4.49985	10880.6	16.09867	38230.4
4.71081	11666.3	16.76752	39595.3
5.59755	12756.6	17.44861	40879.8
5.76547	12995.5	17.72359	41469.1
5.8196	13133.4	18.66955	43332.3
5.82457	13139.9	19.72165	45528.3
5.91682	13404.8	20.30943	46842.3
5.92284	13409.5	20.93754	48475.6
5.95925	13514.6	22.96799	54232.5
5.97106	13520.0	23.80771	56491.1
6.07043	13865.4	25.02729	58983.4
6.08693	13869.7	25.2398	59457.6
6.10433	13921.4	26.65723	64115.1
6.10867	13925.4	27.20113	67172.4
6.16955	14045.5	28.4088	72261.0
6.17969	14050.2	29.65864	76441.3
6.40801	14600.7	30.7944	80271.1
6.43547	14641.6	31.77707	84745.5
6.46152	14648.7	31.94165	85079.8
7.58853	16963.7	33.46412	90253.8
8.16729	18967.6	36.23704	104031.8
11.29749	27545.3	36.3832	104544.2
11.50136	27795.1	36.97086	106809.6
11.94778	28962.7	37.2869	108289.0
13.33011	32523.8	37.90513	110653.1
13.76081	33747.1		

Table S2. Goodness-of-fit statistics (coefficients of determination R^2) of elemental intensities measured by XRF core scanner versus elemental concentrations measured by conventional XRF (Fig. S5).

Element	**R^2**
Al	0.91
Si	0.49
K	0.82
Ca	0.78
Ti	0.89
Mn	0.70
Fe	0.88
Sr	0.76

Table S3. Goodness-of-fit statistics (coefficients of determination R^2) of log ratios of elemental intensities (XRF core scanner) versus concentrations (conventional XRF) (Fig. S5).

	Al	Si	K	Ca	Ti	Mn	Fe	Sr
Al		0.70	0.23	0.98	0.01	0.52	0.48	0.93
Si	0.70		0.25	0.92	0.59	0.42	0.51	0.82
K	0.23	0.25		0.94	0.01	0.57	0.27	0.89
Ca	0.98	0.92	0.94		0.99	0.85	0.98	0.34
Ti	0.01	0.59	0.01	0.99		0.68	0.77	0.96
Mn	0.52	0.42	0.57	0.85	0.68		0.63	0.87
Fe	0.48	0.51	0.27	0.98	0.77	0.63		0.95
Sr	0.93	0.82	0.89	0.34	0.96	0.87	0.95	

Table S4. Operating conditions of the Laser and the quadrupole ICP-MS and list of measured isotopes.

Laser ablation		
	Laser type	GeoLas C, Lambda Physics Compex 100, 193 nm
	Scan length (mm)	4.6
	Energy density (J cm^{-2})	4.7
	Crater size (μm)	160x160
	Repetition rate (Hz)	10
	Scanning speed (μm s^{-1})	20
	Cell	Sedimentcell (LDHCLA)
ICP-MS		
	Instrument	Agilent 7500 cs
	RF power (W)	1500
	Carrier gas >>He (L min-1)	1
	Nebulizer gas, (L min-1	0.79
	Aux. Gas, Ar (L min^{-1})	0.84
	Plasma gas, Ar (L min^{-1})	17
	Dwell time (ms)	10
	Sweep time (ms)	560
NIST 612: 12C, 13C, 23Na, 25Mg, 26Mg, 27Al, 29Si, 30Si, 31P, 34S, 35Cl, 39K, 42Ca, 44Ca, 45Sc, 47Ti, 51V, 52Cr, 53Cr, 55Mn, 56Fe, 57Fe, 62Ni, 63Cu, 66Zn, 79Br, 85Rb, 86Sr, 88Sr, 89Y, 90Zr, 93Nb, 95Mo, 127I, 135Ba, 137Ba, La138, 139La, 140Ce, 141Pr, 146Nd, 147Sm, 151Eu, 153Eu, 165Ho, 166Er, 178Hf, 208Pb, 232Th, 238U		

Table S5. Branched and Isoprenoid Tetraether (BIT) index for samples of core MD03-2621 (Fig. S4).

Sample Name	section (m)		depth within section		uncorr. Depth (mbsf)	BIT
	Top	Bot	Top	Bot		
CA-1	3.0	4.5	87.4	88.4	3.879	0.03
CA-2	4.5	6.0	127.4	128.3	5.7785	0.02
CA-3	6.0	7.5	36.9	37.9	6.374	0.05
CA-4	7.5	9.0	6.6	7.6	7.571	0.07
CA-5	7.5	9.0	123.8	124.6	8.742	0.04
CA-6	9.0	10.5	95.6	96.6	9.961	0.04
CA-7	12.0	13.5	13.8	14.8	12.143	0.06
CA-8	12.0	13.5	142.4	143.4	13.429	0.07
CA-9	13.5	15.0	78	79	14.285	0.05
CA-10	15.0	16.5	44.1	44.9	15.445	0.05
CA-11	16.5	18.0	84.5	85.5	17.35	0.05
CA-12	18.0	19.5	17.1	17.9	18.175	0.07
CA-13	18.0	19.5	71.3	72.3	18.718	0.05
CA-14	19.5	21.0	102.3	103.3	20.528	0.08
CA-15	21.0	22.5	17.7	18.7	21.182	0.09
CA-16	21.0	22.5	102.5	103.5	22.03	0.06
CA-17	22.5	24.0	12.2	13.2	22.627	0.06
CA-18	24.0	25.5	60.8	61.8	24.613	0.08
CA-19	24.0	25.5	128.7	129.7	25.292	0.07
CA-20	25.5	27.0	88.4	89.4	26.389	0.07
CA-21	27.0	28.5	14.5	15.5	27.15	0.06
CA-22	28.5	30.0	52.3	53.1	29.027	0.07
CA-23	28.5	30.0	54.7	55.7	29.052	0.07
CA-24	28.5	30.0	112	113	29.625	0.06
CA-25	30.0	31.5	122	122.9	31.2245	0.07
CA-26	37.5	39.0	10.2	11.2	37.607	0.08
CA-27	42.0	43.5	131	132	43.315	0.08
CA-28	43.5	45.0	63.7	64.7	44.142	0.09
CA-29	45.0	46.5	116.3	117.3	46.168	0.04
CA-30	46.5	48.0	38.4	39.4	46.889	0.09